Spherical Shallow Water Waves Waves Simulation by a Cubed Sphere Finite Difference Solver

Matthieu Brachet, Jean-Pierre Croisille

SPHERICAL SHALLOW WATER WAVES SIMULATION BY A CUBED SPHERE FINITE DIFFERENCE SOLVER

M. BRACHET†AND J.-P. CROISILLE‡

Abstract. We consider the test suite for the Shallow Water (SW) equations on the sphere suggested in [28, 29]. This series of tests consists of zonally propagating wave solutions of the linearized Shallow Water (LSW) equations on the full sphere.

Two series of solutions are considered. The first series [28] is referred to as "barotropic". It consists of an extension of the Rossby-Haurwitz test case in [35]. The second series [29] referred to as (Matsuno) "baroclinic", consists of a generalisation of the solution to LSW in an equatorial chanel introduced by Matsuno [18].

The Hermitian Compact Cubed Sphere (HCCS) model which is used in this paper is a Shallow Water solver on the sphere introduced in [4]. The spatial approximation is a center finite difference scheme based on high order differencing along great circles. The time stepping is performed by the explicit RK4 scheme or by an exponential scheme. For both test case series, barotropic and baroclinic, the results show a very good agreement of the numerical solution with the analytic one, even for long time simulations.

Keywords: Spherical Shallow Water waves - Inertia-gravity wave - Rossby wave - Cubed Sphere grid - Finite difference scheme - Exponential time scheme

1. Introduction

In this paper we consider the Shallow Water equations (SW) on a rotating sphere. These equations serve as a reference system to be solved to assess the accuracy of dynamical cores for meteorology in spherical geometry [10]. The linearized version of SW at an atmosphere at rest is called the LSW system. It represents the minimal wave model of interest on the rotating sphere. It is of foremost importance in climatology and oceanography. As mentioned in the monograph [20], LSW is still a topic with many open problems. One of these problems is the derivation of quasi-analytic solutions to LSW. Such solutions are natural candidates to serve as global test cases for SW. Along this line, two new series of test cases for SW have been recently suggested in [28, 29].

The goal of this paper is to assess a particular finite difference method on the sphere using these two series of test cases. The finite difference scheme under consideration uses the equiangular Cubed Sphere [25]. This scheme, called HCCS, [1] can be seen as an extension to the Cubed Sphere of the 4th order compact scheme, widely used in Computational Aeroacoustics (CAA) [36]. The HCCS scheme for the SW equation has been considered in [4, 3] and in [6, 7] for the linear convection equation. Very good accuracy and stability properties were observed for a broad series of test cases [34, 9, 24]. As in the spectral method, although the design of the spatial approximation is not ab initio conservative, excellent conservation properties are numerically observed.

The purpose of the test cases for SW suggested in [28, 29] is to assess the accuracy of dynamical cores for long time simulations. The physical and mathematical analysis of the test cases can be found in [8, 21] and in [26, 27]. The family of solutions that are derived are doubly quantified with a couple of integers (k, n). These integers stand for, respectively, the longitudinal wave number, which determines the wave periods in the zonal direction, and the latitudinal mode number, which determines the number of zero crossings in the meridional direction. Along the meridional direction, depending on the case, either the Gegenbauer or the Hermite polynomial functions are involved. [2] Both test cases can be considered as new versions of the well

Date: February 17, 2020.

[1] HCCS stands for Hermitian Compact Cubed Sphere

[2] In contrast, for Spherical Harmonics, the associated Legendre polynomials are involved, see e.g. [1]

known Rossby-Haurwitz test in [35]. The first test case is concerned with the barotropic context, (thick atmosphere layer, "fast" inertia-gravity waves). The second test is concerned with the baroclinic context, (thin atmosphere layer, "slow" inertia-gravity waves). For these two tests, the emphasis is on the fact that a dynamical core must be able to maintain stability and accuracy, even after a very large number of time iterations.

In the present paper, we show that the recently introduced HCCS solver [4] is able to accurately calculate each of these tests. In all cases, the simulated final time corresponds to many wave periods, in particular for the Rossby type solutions.

The outline of the paper is as follows. In Section 2 we recall the principle of the spherical approximation with the HCCS scheme. In Section 3, we summarize the derivation of the quasi-analytical solutions for LSW, as presented in [26, 27]. The set up of both test cases with the HCCS formalism is given in Section 4. The numerical results for the barotropic and the baroclinic cases are reported in Section 5 and Section 6 respectively. Conservation properties are reported in detail in Section 7. Concluding remarks ans perspectives are given in Section 8.

2. The HCCS solver: a Cubed Sphere approximation for the Spherical Shallow Water equations

In this section, the Hermitian Compact Scheme on the Cubed Sphere (HCCS) is summarized [6, 7, 3, 4]. Consider the spherical Shallow Water equations (SW):

$$\text{(SW)}\begin{cases} \dfrac{\partial h^\star}{\partial t}(t,\mathbf{x}) + \nabla_T \cdot (h^\star(t,\mathbf{x})\mathbf{u}(t,\mathbf{x})) = 0, \\ \dfrac{\partial \mathbf{u}}{\partial t}(t,\mathbf{x}) + \nabla_T \left(\dfrac{1}{2}|\mathbf{u}(t,\mathbf{x})|^2 + gh(t,\mathbf{x})\right) + (f(\mathbf{x}) + \zeta(t,\mathbf{x}))\,\mathbf{n}(\mathbf{x}) \times \mathbf{u}(t,\mathbf{x}) = \mathbf{0}. \end{cases} \tag{1}$$

In (1), the unknown is $(t,\boldsymbol{x}) \in \mathbb{R}_+ \times \mathbb{S}_a \mapsto q(t,\mathbf{x}) = [h(t,\boldsymbol{x}), \boldsymbol{u}(t,\boldsymbol{x})]^T$, with h the height of the atmosphere and $\boldsymbol{u}$ the tangential wind velocity. The *relative vorticity* is $\zeta = (\nabla_T \times \mathbf{u}) \cdot \mathbf{n}$ and $h^\star(t,\boldsymbol{x}) = h(t,\boldsymbol{x}) - h_s(\boldsymbol{x})$ with h_s the bottom topography function. The subscript T denotes tangential operators. The Coriolis force is $f(\boldsymbol{x}) = 2\Omega\sin(\theta)$, where θ is the latitude angle and Ω the angular earth velocity. Equation (1) is rewritten as

$$\partial_t q(t,\boldsymbol{x}) = F(q(t,\boldsymbol{x})), \tag{2}$$

where $\boldsymbol{q}(\boldsymbol{x}) \mapsto F(\boldsymbol{q})(\boldsymbol{x})$ denotes

$$F(\boldsymbol{q})(\boldsymbol{x}) = -\begin{bmatrix} \nabla_T \cdot (h^\star \mathbf{u}) \\ \nabla_T \left(\dfrac{1}{2}|\mathbf{u}|^2 + gh\right) + (f+\zeta)\,\mathbf{n} \times \mathbf{u} \end{bmatrix}. \tag{3}$$

Consider a function $\boldsymbol{q}(t,\boldsymbol{x}) = \bar{\boldsymbol{q}} + \boldsymbol{q}'(t,\boldsymbol{x})$, with $\bar{\boldsymbol{q}} = [\bar{\boldsymbol{h}} = \boldsymbol{H}, \bar{\boldsymbol{u}} = \mathbf{0}]^{\boldsymbol{T}}$ an atmosphere at rest with fixed height H. The perturbation is $\boldsymbol{q}'(t,\boldsymbol{x})$:

$$\boldsymbol{q}'(t,\boldsymbol{x}) = [h'(t,\boldsymbol{x}), \boldsymbol{u}'(t,\boldsymbol{x})]^T, \quad \boldsymbol{u}' = [u', v']. \tag{4}$$

With the notation

$$\bar{\boldsymbol{J}} = J_{\alpha,\beta} = \partial_\beta F_\alpha(\bar{\boldsymbol{q}}), \quad \alpha,\beta = 1,\ldots,3, \tag{5}$$

the linearization of (2) at $\bar{\boldsymbol{q}}$ is

$$\partial_t q'_\alpha(t,\boldsymbol{x}) = \bar{J}_{\alpha\beta} q'_\beta(t,\boldsymbol{x}), \quad \text{(summation over } \beta\text{)}, \tag{6}$$

or equivalently

$$\text{(LSW)}\begin{cases} \dfrac{\partial h'(t,\mathbf{x})}{\partial t} + H\nabla_T \cdot \mathbf{u}'(t,\mathbf{x}) = 0, \\ \dfrac{\partial \mathbf{u}'(t,\mathbf{x})}{\partial t} + g\nabla_T h'(t,\mathbf{x}) + f(\mathbf{x})\mathbf{n}(\mathbf{x}) \times \mathbf{u}'(t,\mathbf{x}) = 0. \end{cases} \tag{7}$$

The HCCS scheme provides an approximation in space of (1). It is based on the equiangular Cubed Sphere, which is a particular grid of the sphere. This grid is decomposed in six panels matching the six faces of a cube [25]. A typical panel is shown in Fig. 1. In recent years, Cubed Sphere grids have become a standard in numerical climatology. Different kinds of Cubed Spheres do exist [23]. Cubed Spheres are commonly used as a tiling of the sphere for conservative approximations. In this case, the cells defined by the Cubed Sphere serve for discrete averaging. Examples of conservative approximations on the Cubed Sphere include the finite volume method [32], the discontinuous Galerkin method [2] and the spectral element method [11]. In the contrary, in our case, the nodes of the Cubed Sphere serve as unknown location for finite differencing. The nodes are denoted by

$$\left\{ \begin{array}{l} \boldsymbol{s}_{i,j}^k, \quad k=(I),(II),...(VI) = \text{panel index}, \\ -N/2 \leq i,j \leq N/2 = \text{ horizontal and vertical index.} \end{array} \right. \tag{8}$$

Let $\boldsymbol{q}(\boldsymbol{x})$ be a function defined for $\boldsymbol{x} \in \mathbb{S}_a$, ($a$ = earth radius). A gridfunction approximating $\boldsymbol{q}$ is denoted by $\mathfrak{q} = [\mathfrak{q}_{i,j}^k]^T$ with

$$\boldsymbol{q}(\boldsymbol{s}_{i,j}^k) \simeq \mathfrak{q}_{i,j}^k, \quad k=(I),(II),...(VI), \quad -N/2 \leq i,j \leq N/2. \tag{9}$$

In the HCCS scheme, advantage is taken of coordinate lines of the equiangular Cubed Sphere. These coordinate lines are sections of great circles along which finite differencing is operated. The finite differencing is the standard fourth order (compact) scheme which reads

$$\frac{1}{6}u_{\xi,j-1} + \frac{2}{3}u_{\xi,j} + \frac{1}{6}u_{\xi,j+1} = \frac{u_{j+1}-u_{j-1}}{2\Delta\xi}, \tag{10}$$

where $\xi \in [0, 2\pi)$ stands for an angle along a great circle and $\Delta\xi = 2\pi/N$ is the angular step size. This permits to define centered approximations to the gradient, the divergence and the curl, denoted with subscript Δ:

$$\nabla_T h(\boldsymbol{s}_{i,j}^k) \simeq \nabla_{T,\Delta}\mathfrak{h}(\boldsymbol{s}_{i,j}^k), \quad \nabla_T.\boldsymbol{u}(\boldsymbol{s}_{i,j}^k) \simeq \nabla_{T,\Delta}.\mathfrak{u}(\boldsymbol{s}_{i,j}^k), \quad \nabla_T \times \boldsymbol{u}(\boldsymbol{s}_{i,j}^k) \simeq \nabla_{T,\Delta} \times \mathfrak{u}(\boldsymbol{s}_{i,j}^k). \tag{11}$$

The analytical solution $\boldsymbol{q}(t,\boldsymbol{x}) = [h(t,\boldsymbol{x}), \boldsymbol{u}(t,\boldsymbol{x})]^T$ is approximated by the numerical solution

$$\mathfrak{q}(t) = [\mathfrak{h}_{i,j}^k(t), \mathfrak{u}_{i,j}^k(t)]^T, \quad k=(I),(II),...(VI), \quad -N/2 \leq i,j \leq N/2. \tag{12}$$

The discrete system for $\mathfrak{q}(t)$ is deduced from (1) by

- replacing $\boldsymbol{q}(t,\boldsymbol{x})$ by $\mathfrak{q}(t)$.
- replacing all differential operators ∇_T by their discrete approximations $\nabla_{T,\Delta}$ defined in (11).

This provides the semi-discrete HCCS solver, which reads

$$\partial_t \mathfrak{q}(t) = F_\Delta(\mathfrak{q}(t)), \tag{13}$$

where $F_\Delta(\mathfrak{q})$ is defined by

$$F_\Delta(\mathfrak{q}) = F_\Delta([\mathfrak{h}_{i,j}^k, \mathfrak{u}_{i,j}^k]^T) = -\begin{bmatrix} \nabla_{T,\Delta} \cdot \left[\mathfrak{h}_{i,j}^{\star k}\mathfrak{u}_{i,j}^k\right]^T \\ \nabla_{T,\Delta}\left[\frac{1}{2}|\mathfrak{u}_{i,j}^k|^2 + g\mathfrak{h}_{i,j}^k\right]^T + \left[(f_{i,j}^k + \zeta_{i,j}^k)\mathbf{n}_{i,j}^k \times \mathfrak{u}_{i,j}^k\right]^T \end{bmatrix}. \tag{14}$$

In (14), $\zeta_{i,j}^k = \left(\nabla_{T,\Delta} \times \mathbf{v}_{i,j}^k\right) \cdot \mathbf{n}_{i,j}^k$ is the semi-discrete relative vorticity. The main properties of the HCCS solver, reported in [4], are the following:

- It is fully centered for the vector $\mathfrak{q}_{i,j}^k$.
- It is fourth order accurate with respect to $\Delta = \Delta\xi = \Delta\eta$, where (ξ,η) stands for the local coordinate system on a panel.

Several time stepping schemes have been proved to be efficient to integrate (14) in time. Specifically in this paper, we display results obtained with two time schemes. First the explicit RK4 scheme is used, subject to a stability condition CFL ≤ 1. The second time stepping is a particular exponential scheme of the Rosenbrock family, [12, chap.7], referred as ERK2 in the sequel. Several studies have found this scheme as a relevant option for spherical SW problems. Refer to [5, 4]. The efficiency of the ERK2 scheme for the test series presented is confirmed here. In all cases a spatial filtering is added at each time step. This filter consists in

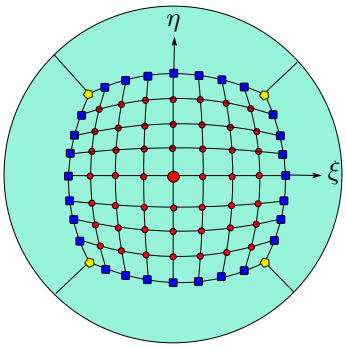

FIGURE 1. The points of a typical panel of the Cubed-Sphere are classified in three categories as follows: (i) the $(N-1)^2$ circles correspond to the *internal* points; (ii) the $4(N-1)$ squares correspond to the *edge* points ; (iii) the 4 pentagons correspond to the *corner* points. The coordinate system consists of the two "equatorial" angles (ξ, η), $-\pi/4 \leq \xi, \eta \leq \pi/4$, with origin at the panel center. The angles ξ is analog to the longitude angle λ. The angle η is also a "longitude" angle, deduced from ξ by a 90 degrees rotation.

an hyperdiffusion term operated along the great circles of the Cubed Sphere. This hyperdiffusion step has been found a suitable way to enhance stability without destroying high accuracy. Details on recent results with the HCCS solver and various time steppings are reported in [4].

3. LSW solutions as approximations of SW equations

3.1. **Zonally propagating waves.** Assessing accuracy and stability of dynamical cores with suitable test cases has become an essential task in numerical meteorology. A well known test series for SW over the sphere is [35]. This test series is a standard that any SW solver must successfully pass. Number 6 in [35] is the well known Rossby-Haurwitz (RH) test case. This test consists in comparing the SW solution to an analytically known solution of the non divergent barotropic equation (BV). The goal is to observe how the numerical code at hand behaves when simulating the hydrodynamics mode. However, since the BV equation is not the SW equation, when using the initial data of test 6 of [35] in a SW solver, acoustic waves are superimposed to the hydrodynamics mode. Thus one does not expect a numerical behaviour conforming to the exact solution of the BV equation: in fact, numerical evidence has shown [30, 20, 33] that the RH initial data evolves in an instability when plugged in a SW numerical solver. As observed in [33], the time of apparition of the instability depends on the particular approximation in space. This instable behaviour was also observed with the HCCS solver [4].

This makes the RH test case not suitable to evaluate a SW solver over long times. Overcoming this flaw was the main purpose for introducing a new series of test cases. In [28, 29], the idea is to consider a zonally propagating simple wave solution of (6) of the form:

$$\boldsymbol{q}'(t, \boldsymbol{x}) = \tilde{\boldsymbol{q}}(\theta) \exp(ik(\lambda - Ct)). \tag{15}$$

In (15), (λ, θ) is the lon-lat coordinate and k is the wave number in the zonal direction, C is a velocity parameter and $\tilde{\boldsymbol{q}}(\theta) = [\tilde{h}(\theta), \tilde{u}(\theta), \tilde{v}(\theta)]^T$ is the amplitude depending on the latitude only. Substituting (15) in (6) leads to the following spectral problem for the LSW equation, which reads:

$$J(\tilde{\boldsymbol{q}}(\theta)) = -ikC\tilde{\boldsymbol{q}}(\theta). \tag{16}$$

The spectral problem (16) contains the amplitude $\theta \mapsto \tilde{\boldsymbol{q}}(\theta)$ and the constant C as unknowns. This is solved by a dispersion analysis. Let the zonal wavenumber k be fixed. The corresponding possible values of the couple eigenvalue/eigenvector are found. In the geophysical context, such a spectral analysis is commonly performed assuming specific a priori hypothesis. Typically, one may assume propagation in an equatorial or midlatitude channel, and the $\beta-$ plan for the Coriolis force. Here there is no such assumption. The

eigenfunction $\tilde{\boldsymbol{q}}(\boldsymbol{x})$ in (16) is defined *on the full sphere*: the latitude angle $\theta \in (-\pi/2, \pi/2)$ extends up to the poles and is not limited to a channel. In the course of this analysis, one could expect to see emerge in one form or another the set of orthogonal eigenfunctions associated to LSW, which is known as the set of *Hough functions*. This is the canonical set of eigenfunctions associated to (7). This system has been studied by many authors [3]. However, due to the lack of closed form, the Hough functions are difficult to use in practice. Refer to [15, 16] for an attempt to use them for defining (quasi-)exact solutions to LSW.

3.2. **Meridional Schrödinger equation.** In a series of works [8, 21], Paldor *et al.* suggested to solve the eigenproblem (16) as follows. The problem is approximated by a differential equation along the meridional direction $\theta \in (-\pi/2, \pi/2)$. This equation is of Schrödinger type. It is expressed as

$$\frac{d^2}{d\theta^2}\psi(\theta) + F(k, C, \theta)\psi(\theta) = 0, \quad \theta \in (-\pi/2, \pi/2), \quad \psi(\pm\pi/2) = 0. \tag{17}$$

In (17), the unknown is the function $\psi(\theta)$. The three components of the vector amplitude $\tilde{\boldsymbol{q}}(\theta) = [\tilde{h}(\theta), \tilde{u}(\theta), \tilde{v}(\theta)]^T$ are expressed explicitely in terms of $\psi(\theta)$. The equation (17) leads to a quantification with two integers k and n corresponding to the zonal and latitudinal behaviour. As already mentioned, k stands for a longitudinal wave number and n for a number of zero crossings in the meridional direction. These two parameters are here independent. This is in contrast to the standard representation of the Spherical Harmonics, where k and n are related by $|k| \leq n$. For each couple (k, n), the characteristic equation of (17) leads to three distinct phase speeds. These speeds are identified as

- two inertia-gravity waves (propagating eastward and westward)
- a Rossby wave

This is of course no surprise, since in most wave analysis, whatever the particular a priori hypothesis are, these three kinds of waves emerge.

A second step in the spectral analysis of (17) in [26, 27] is to give a suitable approximation of the wave speeds and of the eigenfunctions. The idea is to expand the amplitude $\tilde{q}(\theta)$ in a discrete basis of orthogonal polynomials. This leads to an approximation which is considered as quasi-exact. How to select a relevant set of polynomials is based on the physical wave regime. Two cases of interest are emphasized, the "thick ocean" and the "thin ocean" regimes, respectively.

(1) **Thick ocean regime** [27]: This regime corresponds in (7) to a depth with magnitude $H \simeq 1000$m. It is referred to as "barotropic". It corresponds to "fast" acoustic (inertia-gravity) waves with velocity of magnitude $100\mathrm{m\,s}^{-1}$.

(2) **Thin ocean regime** [26]: This regime corresponds in (7) to a depth with magnitude $H \simeq 10$m. It is referred to as *baroclinic*. This corresponds to slow acoustic waves with velocity of magnitude $10\mathrm{m\,s}^{-1}$. This is a more "hydrodynamic" regime. This corresponds to an amplitude function localized near the equator, vanishing close to the poles.

In general, the validity of the approximations provided by (15)-(17) depend on the values of k, n and H. Let us only mention here that for moderate values of k and n, the thick ocean regime becomes valid for large values of H of the order of 1000 m or more. A detailed discussion on the choice of polynomial approximations using either the Gegenbauer polynomials or the Hermite polynomials, is presented in [28, 29].

Remark 3.1. As in Matsuno [18], the resolution of (17) provides three roots corresponding to three kinds of waves. But, whereas in [18] the dispersion analysis is considered in an equatorial channel (and with the $\beta-$plan hypothesis), it is considered here on the full sphere.

3.3. **Design of the numerical test cases.** Distinguishing these two physical regimes led to the design of two series of test cases introduced in [28] and [29] respectively. These tests aim to give a standardization of two particular solutions of the form (15). The main idea on which these two test suites are based is that spherical waves must be approximated with high fidelity by dynamical core models. This underlines the importance of the "pure wave regime" for numerical meteorology and climatology [19]. The emphasis for these test cases is on accurately evaluating the dispersion and dissipation properties of the numerical method

[3] Longuet-Higgins [17] is a well known reference on this topic

to be assessed, in particular over a long physical time. The notation for the tests and for the error analysis is given in Section 4. There are four tests in all. In Section 5, the results with the HCCS solver are displayed for the first test case (barotropic waves). The tests for the thick ocean regime are called Test 1-a (EIG wave) and Test 1-b (Rossby wave). In Section 6, the results for the baroclinic waves are presented, with Test 2-a (EIG wave) and Test 2-b (Rossby wave). To assess the accuracy and stability of the spatial approximation, both cases are considered with different time stepping schemes. Our numerical results were obtained with the explicit RK4 scheme and with a particular exponential scheme (the ERK2 Rosenbrock scheme). [4]

4. Test case setting and numerical notation

4.1. **Setting up the test cases.** The implementation of the two series of test cases presented in Section 3.3 proceeds as follows. Test 1 and Test 2 series correspond to the barotropic and the baroclinic waves respectively. Each series contains an eastward propagating inertia gravity wave referred to as "Test 1-a EIG" (barotropic) and "Test 2-a EIG" (baroclinic) waves respectively. The Rossby wave in each series is referred to as "Test 1-b Rossby" (barotropic) and "Test 2-b Rossby" (baroclinic) respectively. In all cases, the analytic solutions is of the form (15) where parameters specifying the function $q'(t, \boldsymbol{x})$ in (15) are

(1) The depth H of the atmosphere at rest.
(2) The zonal wave number k and mode number n.
(3) The wave number k is the wavenumber along the zonal direction λ, (longitude direction). The mode number n corresponds to the meridional direction θ (latitude direction). The analytic solution involves for the meridional modulation a Gegenbauer polynomial in the barotropic case and a Hermite polynomial in the baroclinic case. The dispersion analysis with the eigenmodes and the (vector) eigenfunctions is given in [26, 27] and is not reproduced here. In the Test 1 and and Test 2 series, we have used the routines provided as supplementary material in [28, 29] respectively [5]. The routines calculate the analytic solutions in the four cases (1a, 1b, 2a and 2b). In all cases, the constants in front of the amplitude must be chosen small enough to ensure that the wave (15) be effectively a (quasi) analytic solution.
(4) In all cases, the numerical solver is the HCCS scheme (13). The initial data at $t = 0$ is the analytic value given by the matlab routine. It is evaluated at $t = 0$ at the nodes $\boldsymbol{s}^k_{i,j}$ of the Cubed Sphere. As already mentionned, the time stepping is performed using various time schemes for comparison. The explicit fourth order RK4 is our reference scheme. The second order Rosenbrock scheme ERK2 was used as well. Refer to [5, 4] for comments on using these time schemes in the context of the SW equations (1).

4.1.1. *Test Case 1: barotropic waves.* The input parameters are selected as follows:

- The atmosphere mean depth is:

$$H = 5000\text{m}. \tag{18}$$

- The wave numbers k (zonal wave number) and n (meridional wave number) are:

$$(k, n) = (5, 10). \tag{19}$$

- The wave solutions are as follows:
  (1) Test 1-a is a barotropic inertia gravity wave. It is an Eastward Inertia Gravity wave called EIG with period 3.16h. Thus 100 periods represent 13.5 days.

  (2) Test 1-b is a barotropic Rossby wave. It has a period of 12.03 days, (100 periods = 1203 days).

The reference Courant number for the EIG wave at the equator is

$$\text{CFL} = \frac{\sqrt{gH}\Delta t}{a\Delta\xi}, \tag{20}$$

[4] This kind of numerical assessment is also used in gas dynamics (Euler or Navier-Stokes sequations). The accuracy of the nonlinear scheme is assessed when used for wave propagation problems, e.g. occuring in aeroacoustics or turbulence.

[5] This supplementary material is also provided in matlab, python and FORTRAN for the Test 1 series and in python for the Test 2 series

where $a = 6371.22$km is the earth radius and $\Delta\xi = a\pi/2N$. The integer N represents the Cubed Sphere resolution. For example, the reference Courant number CFL $= 1$ corresponds with $N = 64$ to a time step of $\Delta t = 699$s.

4.1.2. *Test Case 2: baroclinic waves (Matsuno).* The input parameters are selected as follows:

- Atmosphere mean depth:

$$H = 30\text{m}. \tag{21}$$

- The wave numbers k (zonal wave number) and n (meridional wave number) are

$$(k, n) = (5, 1). \tag{22}$$

The two waves are

(1) Test 2-a is an EIG (Eastward Inertia Gravity) wave. The period is 1.9 days. Thus 100 periods represent 190 days.

(2) Test 2-b is a Rossby wave with a period of 18.5 days, (100 periods = 1850 days).

Compared to (20), the Coriolis force is larger. In this case, the reference Courant number is

$$\text{CFL} = \frac{\Delta t}{a\Delta\xi}\sqrt{gh_0 + \frac{4\Omega^2 a^2 \Delta\xi^2}{6}}. \tag{23}$$

The Courant number CFL $= 1$ corresponds (with a Cubed Sphere resolution $6 \times 64 \times 64$) to a time step $\Delta t = 8013$s. This is 10 times larger than for Test 2-a.

4.2. **Error notation.** In Sections 5 and 6, the shape of the numerical solutions are shown at initial and final times. In addition, various errors between the analytical and the calculated solutions are reported. The analytical solution of (1) is

$$\boldsymbol{q}(t, \boldsymbol{x}) = [h(t, \boldsymbol{x}), \boldsymbol{u}(t, \boldsymbol{x})]^T, \tag{24}$$

where the velocity $\mathbf{u}$ is decomposed in zonal and meridional components as

$$\mathbf{u} = u_\lambda \mathbf{e}_\lambda + u_\theta \mathbf{e}_\theta. \tag{25}$$

The numerical solution (12) is

$$\mathfrak{q}(t) = [\mathfrak{h}^k_{i,j}(t), \mathfrak{u}^k_{i,j}(t)]^T, \quad k = (I), (II), ...(VI), \quad -N/2 \le i, j \le N/2., \tag{26}$$

where the numerical velocity $\mathfrak{u}$ is decomposed as

$$\mathfrak{u} = \mathfrak{u}_\lambda \mathbf{e}_\lambda + \mathfrak{u}_\theta \mathbf{e}_\theta. \tag{27}$$

(1) *Relative errors*: The relative error on each component is

$$\text{err}_\theta = \frac{\|\mathfrak{u}_\theta - u_\theta\|_2}{\|u_\theta\|_2} \text{ and } \text{err}_\lambda = \frac{\|\mathfrak{u}_\lambda - u_\lambda\|_2}{\|u_\lambda\|_2}, \tag{28}$$

where $\|.\|_2$ denotes the l^2 norm. Similarly for relative error on the height h is given by

$$\text{err}_h = \frac{\|h - \mathfrak{h}\|_2}{\|h - H\|_2}, \tag{29}$$

with $\mathfrak{h}$ the numerical total height.

(2) *Dispersion error:* As in any discrete approximation of a convective equation, there is a dispersion error in the HCCS scheme. This dispersion is apparent when one shows the maximum of the error in function of time. In particular, when the scheme is used over 100 periods, the dispersion is visible. In this case, as mentioned in [20], one is more interested in the preservation of the global shape of the wave that is represented by the grid than by the numerical velocity which necessarily slightly differs from the exact one. As suggested in [28], the dispersive error is represented as follows:

- First the maximum error is plotted.

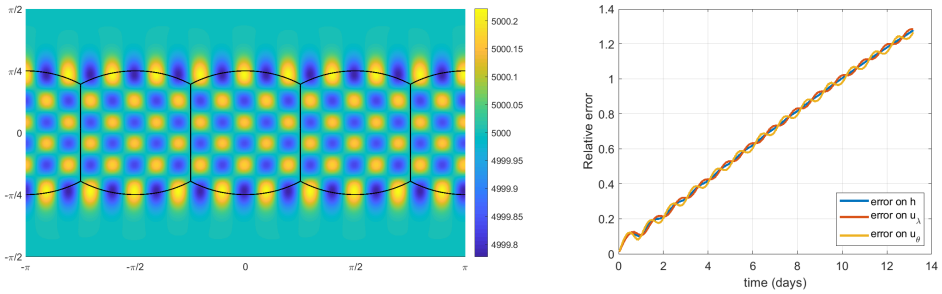

FIGURE 2. Test 1-a (barotropic EIG wave). The final time is $t = 13.5$ days. Left panel: total height at final time. Right panel: Histories of relative errors (28-29) for the zonal velocity is u_λ, the meridional velocity u_θ and the total height h. The time scheme is the ERK2 scheme with 407 time iterations and CFL $= 4$, see (20). The resolution of the Cubed-Sphere is $6 \times 64 \times 64$.

- Second, the dispersion is estimated by the numerical velocity C_n with a Fourier analysis performed on 100 periods and compared to the theoretical velocity C. The relative velocity is defined by

$$|\Delta C| = \frac{|C - C_n|}{|C|} \times 100. \tag{30}$$

- Third, Hovmöller diagrams [13] are given. Such diagrams provide a suitable way to represent the accuracy of a numerical scheme for a propagation phenomenon. There are two variants of Hovmöller diagrams: time/longitude and latitude/time. Both are used in the sequel.

(3) *Dissipation error:* The dissipation is simpler to represent than the dispersion. Here we limit ourselves to plot the history of the extrema of the total height $\mathfrak{h}$. Due to the form (15), the analytical solution obviously does not have any dissipation and the extrema at any time are the extrema at time $t = 0$. Therefore, plotting the minimum and maximum of the numerical solution $\mathfrak{h}$ over a long physical period of time is a simple and reliable way to represent the dissipation of the numerical solver.

5. Test cases 1: barotropic waves

5.1. **Test 1-a: barotropic Eastward Inertia-Gravity (EIG) Wave.** Here, we show numerical results obtained with the HCCS solver for Test 1-a in Section 4.1.1. It is an eastward propagating wave, referred as EIG. In Fig. 2, the left panel displays the total height $\mathfrak{h}$ at time $t = 13.5$ days. The time stepping scheme is the second order accurate Rosenbrock Exponential Integrator (ERK2), [12, chap.7]. Refer to [5, 4] for more details on using ERK schemes for SW equations. The right panel displays the history of the relative error. This error increases in function of time and behaves periodically. This reflects the fact that some error, dispersive and/or dissipative, is necessarily present in any numerical approximation for convection. On this topic, refer to [28]. Still regarding dispersion, the Table 1 reports the magnitude of the relative error on the velocity $|\Delta C|$ defined in (30). In all cases, the magnitude is smaller than 1%. Another representation of the dispersion is given in the left and middle panels in Fig. 3. In the left panel, a time longitude Hovmöller diagram is shown. This diagram is a suitable representation of the characteristics lines of the convection phenomenon at hand (here the EIG wave) emanating from a parallel at a given latitude. The dashed line represents the numerical slope, with CFL $= 1$ (RK4 scheme) and CFL $= 4$ (ERK2 scheme) respectively. A very good alignement of the exact and numerical slope can be observed. In the middle panel, a latitude-time Hovmöller diagram is shown. This second kind of Hovmöller diagram allows to illustrate the temporal changes as opposed to an instantaneous snapshot. Such a representation was used in [29]. Finally in the right panel, the dissipation of the HCCS solver is represented using the history of the extrema (maximum and minimum) of the total height h. As can be observed, the maximum and the miminum values are almost

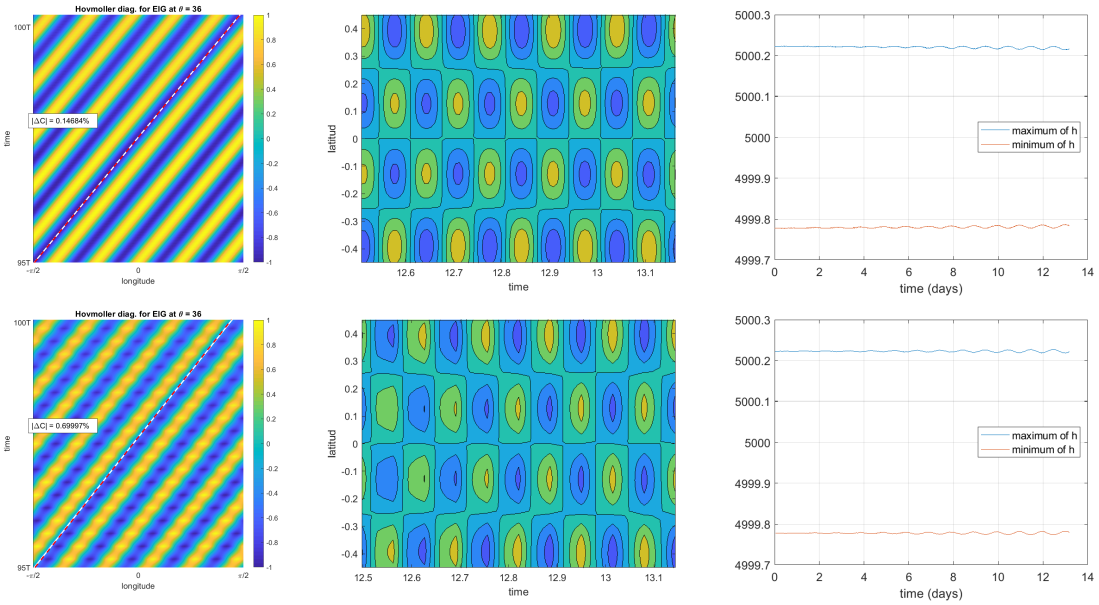

FIGURE 3. Test 1-a (barotropic EIG wave). HCCS solver in space at final time is $t = 13.5$ days. First line : RK4 time scheme at CFL $= 0.9$. Second line, ERK2 scheme at CFL $= 4$. The first column corresponds to time-longitude Hovmöller diagrams of the numerical solutions obtained by intersecting the zonal velocity at latitude $\theta = 36\,\text{deg}$. The second column is corresponds to latitude-time Hovmöller diagrams obtained by intersecting the zonal velocity at longitude $\lambda = -18\text{deg}$. The third column displays the maximum and the minimum history of the total height h over the full simulation. No significant damping is observed. The Cubed-Sphere resolution is $6 \times 64 \times 64$.

constant during 100 time periods. This shows that the center solver HCCS is almost dissipation free in this case.

Time scheme	**Courant Number** CFL	**barotrop. EIG wave**
ERK2	1	0.6389%
	4	0.6999%
	8	0.4405%
RK4	1	unstable
	0.9	0.1468%

TABLE 1. Test 1-a (barotropic EIG wave). Dispersion analysis at final time is $t = 13.5$ days (100 periods). The relative velocity errors $|\Delta C|$ in (30) are reported for various values of CFL. The relative error on the velocity is smaller than 1% in all cases after 100 periods. The RK4 scheme with CFL $= 0.9$ corresponds to 1808 time iterations and the ERK2 time scheme with CFL $= 4$ corresponds to 407 time iterations, see (20). Note that the ERK2 is stable with a CFL number as high as CFL $= 32$. This is not reported in the table since in this case the sample rate is too low to accurately evaluate $|\Delta C|$. The resolution of the Cubed-Sphere is $6 \times 64 \times 64$.

Remark 5.1. The results obtained with a second ERK scheme (the ERK3 scheme), for which we refer to [5, 4], are similar with the RK4 time scheme or with the ERK2 scheme. These results are not reported here. For a given scheme assumed to be stable, the results are not sensible to the value of the Courant number.

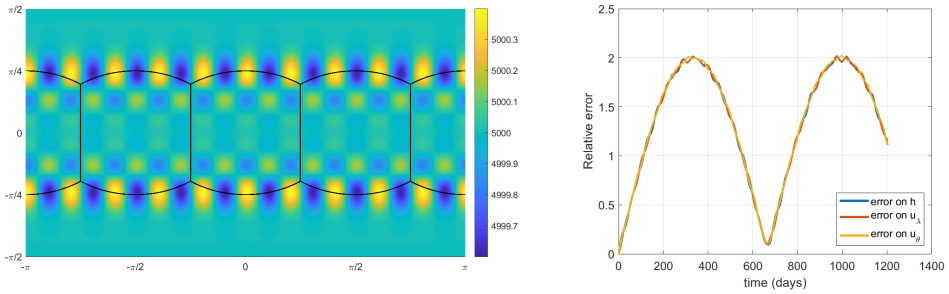

FIGURE 4. Test 1-b (barotropic Rossby wave), HCCS solver in space. The final time is $t = 1203$ days (100 periods). The time scheme is the ERK2 time scheme with 9289 time iterations and CFL $= 16$, see (20). Left panel: total h at final time. Right panel: history of the relative errors for h, u_λ (zonal velocity) and u_θ (meridional velocity). The three curves are almost superposed. The resolution of the Cubed-Sphere is $6 \times 64 \times 64$.

5.2. **Test 1-b: barotropic Rossby Wave.** Here we consider the so called barotropic Rossby wave, whose setup is given in Section 4.1.1. Again the HCCS solver is used to operate the simulation during 100 periods (1203 days). In Fig. 4, left panel, the total height at final time is reported. In the right panel, the maximum error history for h, u_λ, u_θ is reported. As expected, (see [28]), due to a small dispersion error, these errors oscillate periodically. The velocity error is $|\Delta C| = 2.2722\%$ with the ERK2 scheme and a Courant number CFL $= 16$. With the RK4 scheme and a Courant number CFL $= 0.9$, the error is $|\Delta C| = 1.7661\%$. In both cases, this is slightly larger than the results for the EIG wave reported in Table 1. However, the level of the error remains quite good.

As for the EIG wave, we also report in Fig. 5 a dispersion analysis based on the time/longitude and latitude/time Hovmöller diagrams in the left and middle panels respectively. In both cases, the numerical (dashed line) and theoretical slopes are well aligned. The dissipation of the HCCS solver is reported in the right panel using the history of the extrema of the total height over the full simulation (1200 days, 100 periods). As for the EIG wave, this shows that the HCCS is visually dissipation free at final time when using the Cubed Sphere with resolution $6 \times 64 \times 64$.

Remark 5.2. The Cubed Sphere resolution $6 \times 32 \times 32$ is not sufficient in this case and gives a significant dissipation.

6. Test case 2: Matsuno baroclinic waves

In this section, we display numerical results obtained with the HCCS solver in the case of the baroclinic waves test cases presented in Section 4.1.2. As in Section 5, numerical results with the HCCS solver are reported for two waves: an EIG wave (Test 2-a) and a Rossby wave (Test 2-b). The numerical results for the total height $\mathfrak{h}$ for both the EIG and the Rossby waves are shown in Fig. 6. The final time is 190 days and 1850 days, respectively, and corresponds to 100 periods in both cases. The history of the errors is shown in Fig. 7. As in the barotropic test series, the increasing error history expectedly reflects the (small) dispersion of the scheme, see [28]. As before, Figs. 8, 9 report the two Hovmöller, time/longitude and latitude/time, to better visualize the dispersion (left and middle panels). The RK4 and the ERK2 time stepping schemes are compared. The RK4 scheme is used with a Courant number CFL $= 1$ and the ERK2 scheme is used with a Courant number CFL $= 5$. For both time schemes, the dispersion is very good. Note that some irregularities are apparent in the latitude/time Hovmöller diagrams when using the ERK2 scheme. This reflects the choice of the CFL number CFL $= 5$, which is larger than CFL $= 1$. The history of extrema of $\mathfrak{h}$ in the right panels reflects the dissipation. As before, the HCCS solver appears to be dissipation free with the $6 \times 64 \times 64$ Cubed Sphere. Table 2 reports the relative error on the velocity ΔC. Notice that different values of $|\Delta C|$ are obtained whenever different time schemes and different Courant numbers are used. In all cases, the error on $|\Delta C|$ is small, which is the sign of a small numerical dispersion.

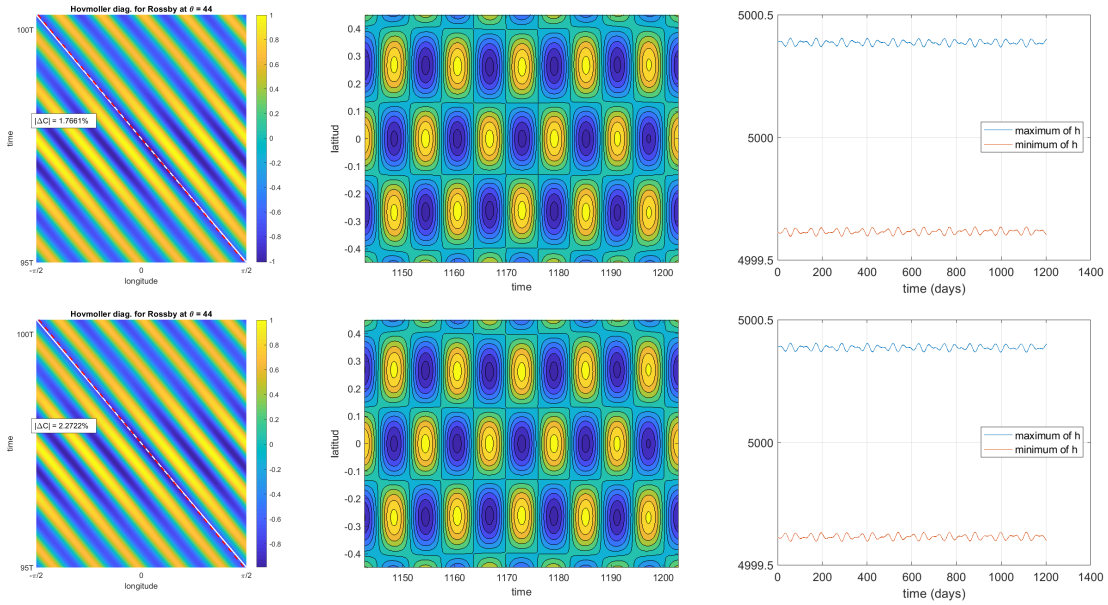

FIGURE 5. Test 1-b (barotropic Rossby wave). Dispersion and dissipation analysis of the HCCS solver at final time (1203 days, 100 periods). First line : RK4 time scheme at CFL = 0.9 and 165143 time iterations. Second line, ERK2 time scheme at CFL = 16 and 9289 time iterations. Left column: time-longitude Hovmöller diagrams of the numerical solutions by intersecting the zonal velocity at $\theta = 44\,\text{deg}$. Middle column: latitude-time Hovmöller diagrams by intersecting the zonal velocity at $\lambda = -18\,\text{deg}$. Right column: dissipation analysis showing the maximum and minimum values of the total h over the full simulation. There is no visible dissipation after 100 periods. The Cubed-Sphere is $6 \times 64 \times 64$.

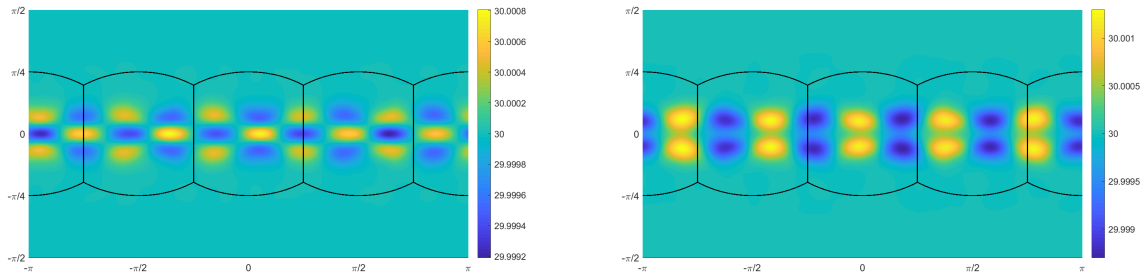

FIGURE 6. HCCS solver in space and the ERK2 time scheme. Left panel: Test 2-a (baroclinic EIG wave). The total height h is shown at final time $t = 190$ days (100 periods) with CFL = 5 and 431 time iterations. Right panel: Test-2b (baroclinic Rossby wave). The total height is shown at final time $t = 1850$ days (100 periods) with CFL = 5 and 4313 time iterations. The solution is more concentrated near the equator than in the barotropic case. The Cubed-Sphere grid is $6 \times 64 \times 64$.

Remark 6.1. In these cases, the resolution of the Cubed Sphere in space for the HCCS solver is $6 \times 64 \times 64$. This is the maximum allowed on our computer. This is below the resolution in [29].

Remark 6.2. The four test cases are performed with a matlab code on a simple laptop. Typical run time are 30min for Test1-a (barotropic EIG wave) 24h for the Test1-b (barotropic Rossby wave), 30min for Test2-a (baroclinic EIG wave) and 5h for the Test2-b (baroclinic Rossby wave) for 100 periods in each case.

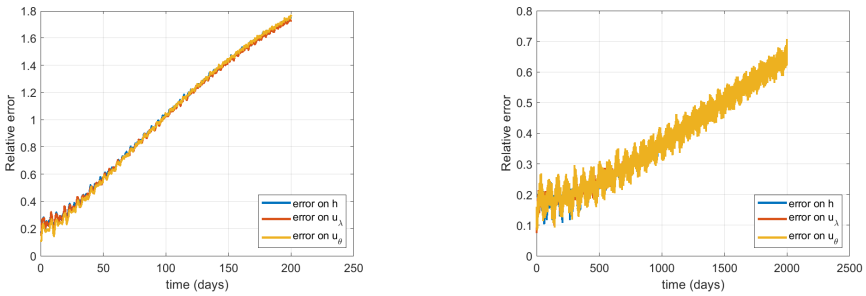

FIGURE 7. Left panel: Test 2-a (baroclinic EIG wave). Right panel: Test 2-b (baroclinic Rossby wave). The HCCS solver in space and the ERK2 time scheme are used in both cases. In both cases, the history of the relative errors for the total height h, the zonal velocity u_λ and the meridional velocity u_θ is shown. For the EIG wave, (left panel), the final time is $t = 190$ days (100 periods) with CFL $= 5$ and 431 time iterations. For the Rossby wave, (right panel), the final time is $t = 1850$ days 9100 periods) with CFL $= 5$ and 4313 time iterations. The Cubed-Sphere grid is $6 \times 64 \times 64$.

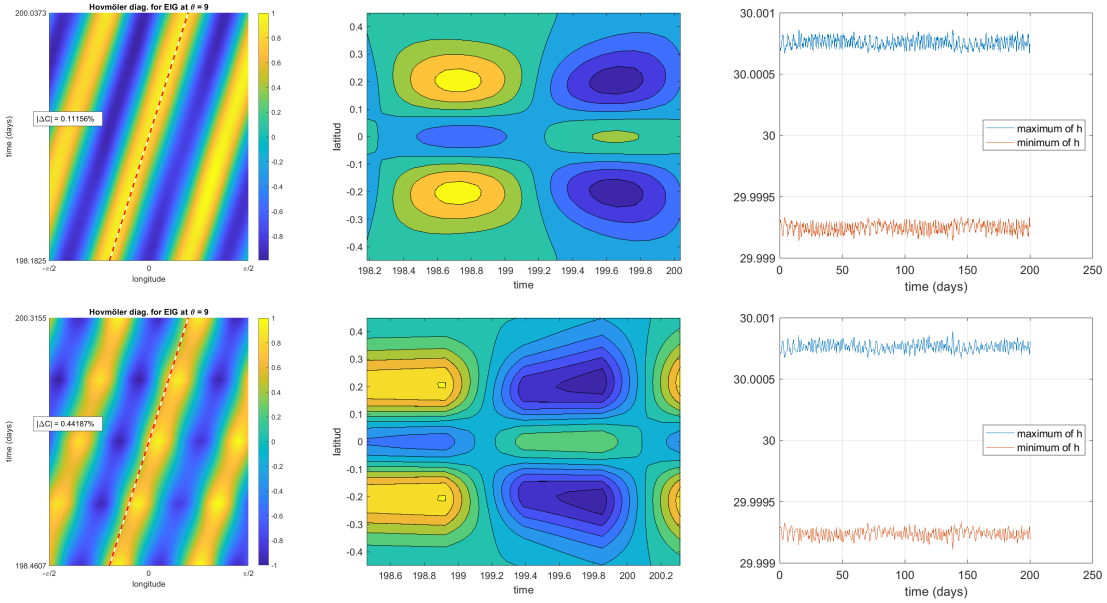

FIGURE 8. Test 2-a (baroclinic EIG wave). The HCCS solver in space is used. First line : RK4 time scheme with CFL $= 1$. Second line, ERK2 time scheme with CFL $= 5$. The first column represents time-longitude Hovmöller diagrams of the simulated solutions obtained by intersecting the zonal velocity at latitude $\theta = 9\,\text{deg}$. The second column is a latitude-time Hovmöller diagram obtained by intersecting the zonal velocity at $\lambda = -18\,\text{deg}$. The third column displays the maximum and minimum values of the total height h over the full simulation (final time: 190 days). The distortion in the middle panel, bottom line, is attributed to the Courant number CFL $= 5$. The Cubed-Sphere is $6 \times 64 \times 64$.

7. CONSERVATION

7.1. **Invariants.** In what follows, the conservation properties obtained in the Test-1 series (Section 5) and in the Test-2 series (Section 6) are numerically analyzed. The constants are $a = 6.37122 \times 10^6\text{m}$ (earth radius),

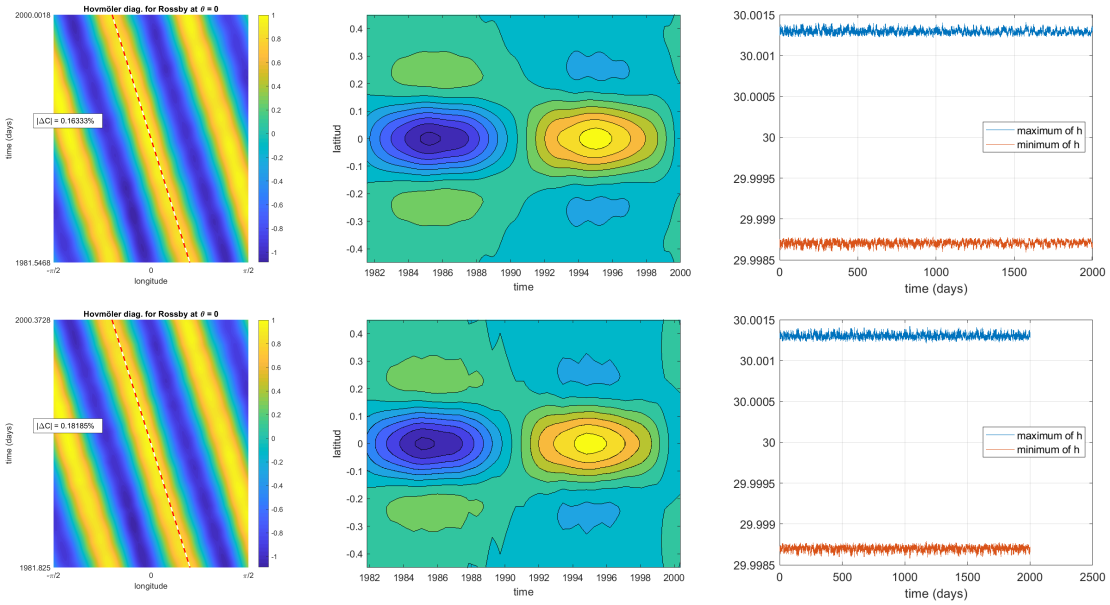

FIGURE 9. Test 2-b (baroclinic Rossby wave). First line : RK4 time scheme with Courant number CFL = 1. Second line, ERK2 time scheme with CFL = 5. The first column displays a time-longitude Hovmöller diagrams of the simulated solutions obtained by intersecting the zonal velocity at $\theta = 0\,\text{deg}$. The second column displays a latitude-time Hovmöller diagrams obtained by intersection the zonal velocity at longitude $\lambda = -18\,\text{deg}$. The third column represents the maximum and minimum values of h over 1850 days (100 periods). The Cubed-Sphere is $6 \times 64 \times 64$.

Time scheme	**Courant Number**	**EIG wave**	**Rossby wave**
RK4	1	0.11156%	0.16333%
ERK2	5	0.44187%	0.18185%
	10	0.44187%	0.28027%

TABLE 2. Test 2-a (baroclinic EIG wave) and Test 2-b (baroclinic Rossby wave). Dispersion analysis. The table reports the relative error $|\Delta C|$ in (30) for the EIG and Rossby waves with the two time schemes RK4 and ERK2. The results are obtained using a Fourier analysis (see [28]). For the EIG wave, the final time is $t = 190$ days, (100 periods). The number of time iterations are 2156 (CFL = 1), 431 (CFL = 5) and 215 (CFL = 10). For the Rossby wave, the final time is $t = 1850$ days (100 periods). The number of time iterations are 21565 (CFL = 1), 4313 (CFL = 5) and 2156 (CFL = 10). The Cubed-Sphere grid is $6 \times 64 \times 64$.

$\Omega = 7.292 \times 10^{-5}\text{s}^{-1}$ (earth angular velocity), and $g = 9.80616\text{m}\,\text{s}^{-2}$ (gravity constant). The Coriolis force is $f(\boldsymbol{x}) = 2\Omega \sin\theta$. The following averaged values are preserved by SW at the continuous level.

$$
\left\{
\begin{array}{l}
\text{mass: } I_1 = \displaystyle\int_{\mathbb{S}_a^2} h^\star d\mathbf{s}, \\
\text{energy: } I_2 = \displaystyle\int_{\mathbb{S}_a^2} \frac{1}{2} h^\star \mathbf{v}^2 + \frac{1}{2} g \left(h^2 - h_s^2\right) d\mathbf{s}, \\
\text{potential enstrophy: } I_3 = \displaystyle\int_{\mathbb{S}_a^2} \frac{(\zeta + f)^2}{2h^\star} d\mathbf{s} \text{ with } \zeta \text{ the relative vorticity }, \\
\text{divergence: } I_4 = \frac{1}{|\mathbb{S}_a|} \displaystyle\int_{\mathbb{S}_a^2} \nabla_T \cdot \mathbf{v} d\mathbf{s}, \\
\text{relative vorticity: } I_5 = \frac{1}{|\mathbb{S}_a|} \displaystyle\int_{\mathbb{S}_a^2} (\nabla_T \times \mathbf{v}) \cdot \mathbf{n} d\mathbf{s}.
\end{array}
\right. \tag{31}
$$

The numerical error for I_1, I_2 and I_3 is reported using the relative (algebraic) value

$$
\frac{I_p(t) - I_p(0)}{I_p(0)}, p = 1, 2, 3. \tag{32}
$$

The value I_4 and I_5 are reported without scaling.

7.2. **Spherical quadrature.** The integral $\displaystyle\int_{\mathbb{S}_a^2} f(\boldsymbol{x}) d\sigma(\boldsymbol{x})$ is approximated by $Q_N(f)$, a particular quadrature rule on the Cubed Sphere. We have used the rule (20) in [22], which is

$$
Q_N(f) = a^2 \sum_{k=(I)}^{(VI)} \sum_{i,j=-N/2}^{N/2} \alpha_{i,j} F(\boldsymbol{s}_{i,j}^k). \tag{33}
$$

We refer to [22] for the definition of the weights $\alpha_{i,j}$. The numerical integrals in (31) are evaluated by (33).

7.3. **Conservation with the HCCS scheme.** Table 3 and Figs. 10, 11, 12 and 13 report the conservation of the five quantities mass, energy, enstrophy, divergence and vorticity at final time for the Test 1 and Test 2 series. It can be observed that the relative conservation error is excellent in the four cases, ranging from computer accuracy in Fig. 12 to 5.10^{-8} in Fig. 11.

	Test case 1		***Test case 2***	
	EIG wave	*Rossby wave*	*EIG wave*	*Rossby wave*
CFL	4	16	5	5
Relative Mass Error	1.7666 (-14)	2.4476 (-8)	2.8297 (-15)	1.6564 (-12)
Relative Energy Error	2.6838 (-14)	4.8947 (-8)	2.2746 (-16)	3.2573 (-12)
Relative Enstrophy Error	2.5541 (-14)	3.0250 (-8)	2.0419 (-14)	2.9696 (-13)
Mean value divergence	1.5840 (-17)	3.6990 (-16)	3.6539 (-20)	6.8451 (-20)
Mean value vorticity	2.9723 (-19)	5.7501 (-25)	9.3416 (-21)	8.3526 (-21)

TABLE 3. Test 1-a, Test 1-b, Test 2-a and Test 2-b: conservation of the values in (31): mass (relative), energy (relative), enstrophy (relative), mean divergence and mean vorticity with the HCCS solver in space with the ERK2 scheme. Test 1-a (barotropic EIG wave): CFL = 4, t = 13.5 days, (100 periods), 407 time iterations. Test 1-b (barotropic Rossby wave): CFL = 16, t = 1203 days, (100 periods), 9289 time iterations. Test 2-a (baroclinic EIG wave): CFL = 5, t = 190 days, (100 periods), 431 time iterations. Test 2-b (baroclinic Rossby wave): CFL = 5, t = 1850 days, (100 periods), 4313 time iterations. In all cases, the conservation properties are very good, ranging from computer accuracy to values less than 5.10^{-8}.

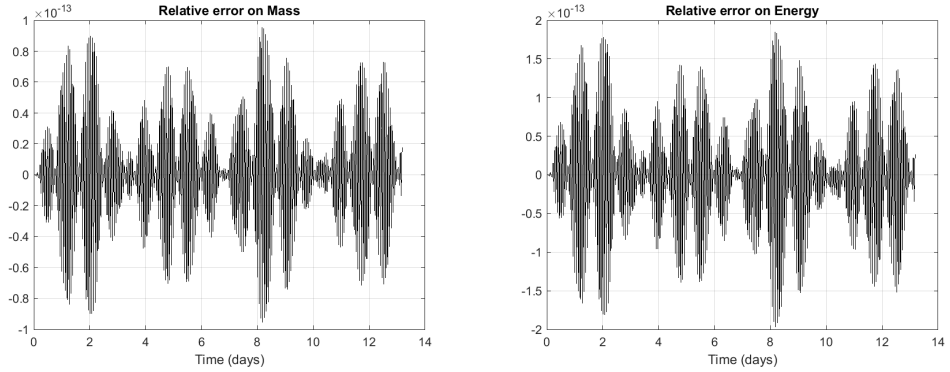

FIGURE 10. Test 1-a (barotropic EIG wave). Left panel: History of the mass relative error (32) for I_1. Right panel: History of the energy relative error (32) for I_2. The solver is the HCCS scheme in space with the ERK2 time scheme with CFL = 4 and 407 time iterations. The conservation accuracy is excellent in all cases, below 2.10^{-13}. The Cubed-Sphere grid is $6 \times 64 \times 64$.

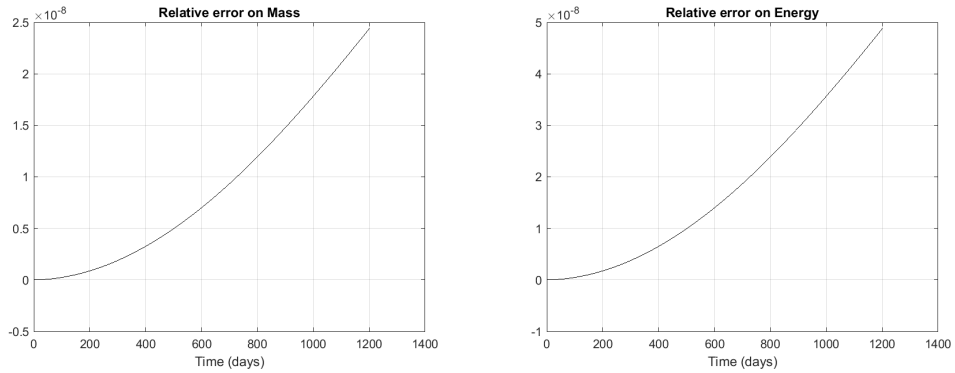

FIGURE 11. Test 1-b (barotropic Rossby wave). Mass and energy relative error (31). HCCS solver in space with ERK2 scheme time scheme with CFL = 16. The conservation accuracy is very good, even after 1203 days, (100 periods) with a level below 5.10^{-8} in both cases. The Cubed-Sphere is $6 \times 64 \times 64$.

8. Concluding remarks

The design of test cases based on SW wave (quasi-)solutions of the equations of meteorology is not a new topic, in 2D or 3D. For a comprehensive history of this approach, refer to [14, 31, 28] and the references therein. The interest of such solutions is multifaceted. Although being academic, these solutions have the advantage to be close to "real" meteorological models. They also have the interest to have a mathematical basis. In fact, such solutions offer an excellent platform for various mathematical aspects of the equations under study. On the one hand, the design of the solutions is interesting in itself. Testing numerical solvers often allows to learn more about the numerical method and its limitation, or about the test case itself. In addition, since very few mathematical results are known on the PDE's (even in the 2D tangential setting), the numerical convergence behaviour of the solver towards "exact" solutions is also a way to learn more.

The two new test series suggested in [28, 29] are a new stimulating family of quasi-analytic solutions of the 2D SW equations. In the present study, they were used to assess the HCCS finite difference solver capability to accurately capture essential features, even after as much as $100,000$ time iterations. The numerical results obtained so far confirm what was already observed in [4]. This was our initial objective. Furthermore, as mentionned above, the solver behaves remarkably well regarding conservation.

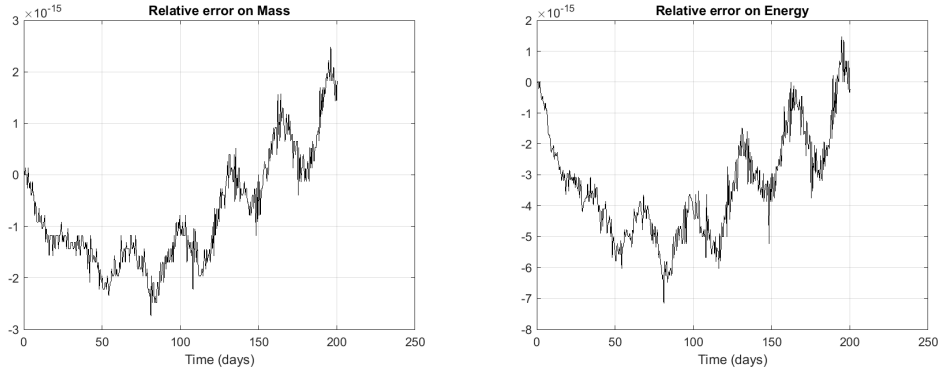

FIGURE 12. Test 2-a (baroclinic EIG wave). HCCS solver in space with the ERK2 time scheme with Courant number CFL = 5. Left panel: Mass relative error. Right panel: Energy relative error. In both case, the level is below 5.10^{-15}, (machine accuracy). The Cubed-Sphere grid is $6 \times 64 \times 64$.

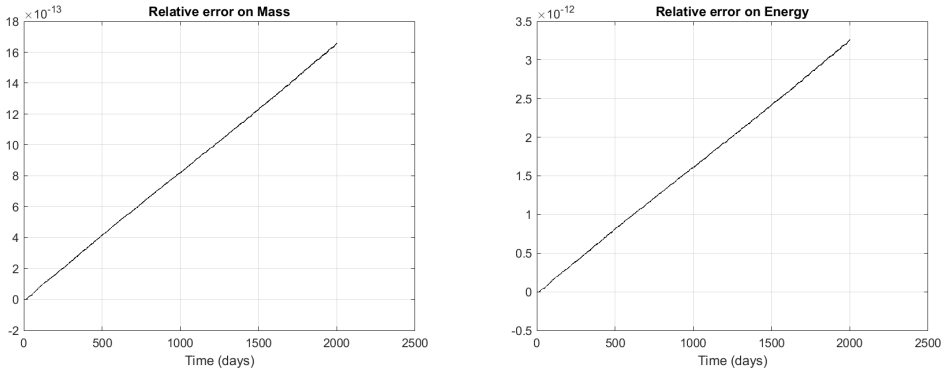

FIGURE 13. Test 2-b (baroclinic Rossby wave). HCCS solver in space with the ERK2 time scheme with Courant number CFL = 5. Left panel: history of the relative mass error. Right panel: history of the relative energy error. 1850 days represent 100 periods. The conservation error is below 5.10^{-12} in both cases. The Cubed-Sphere grid is $6 \times 64 \times 64$.

Clearly, future work is required to complete the mathematical analysis, in particular to analyse the conservation properties observed so far in the wave regime of the spherical SW equations. Finally, extending the HCCS solver to the full 3D SW equations is clearly a desirable perspective.

REFERENCES

[1] K. Atkinson and W. Han. *Spherical Harmonics and Approximations on the Unit Sphere: an introduction*. Number 2044 in Lect. Notes. Math. Springer-Verlag, 2012.

[2] L. Bao, R. D. Nair, and H. M. Tufo. A mass and momentum flux-form high-order discontinuous Galerkin shallow water model on the Cubed-Sphere. *J. Comput. Phys.*, 271:224–243, 2014.

[3] M. Brachet. *Schémas compacts hermitiens sur la sphère: applications en climatologie et océanographie numérique (in french)*. PhD thesis, Univ. Lorraine, 2018.

[4] M. Brachet and J.-P. Croisille. A center compact scheme for the Shallow Water equations on the sphere. 2019, submitted.

[5] C. Clancy and J. A. Pudykiewicz. On the use of exponential time integration methods in atmospheric models. *Tellus A*, 65(1):20898, 2013.

[6] J.-P. Croisille. Hermitian compact interpolation on the Cubed-Sphere grid. *Jour. Sci. Comp.*, 57,1:193–212, 2013.

[7] J.-P. Croisille. Hermitian approximation of the spherical divergence on the Cubed-Sphere. *Jour. Comp. App. Math.*, 280:188–201, 2015.

[8] Y. De-Leon and N. Paldor. Zonally propagating wave solutions of Laplace tidal equations in a baroclinic ocean of an aqua-planet. *Tellus A*, 63:348–353, 2011.
[9] J. Galewsky, R.K. Scott, and L.M. Polvani. An initial-value problem for testing numerical models of the global shallow water equations. *Tellus*, 56:429–440, 2004.
[10] M. Ghil and S. Childress. *Topics in Geophysical Fluid Dynamics:Atmospheric dynamics, Dynamo theory and Climate Dynamics*. Springer, 1987.
[11] F. X. Giraldo. A spectral element shallow water model on spherical geodesic grids. *Int. J. Numer. Meth. Fluids*, 35(8):869–901, 2001.
[12] E. Hairer and G. Wanner. *Solving Differential equations vol. I, II*. Springer Series in Comp. Mathematics. Springer-Verlag, 1991.
[13] E. Hovmöller. The Trough-and-Ridge diagram. *Tellus*, 1(2):62–66, 1949.
[14] C. Jablonowski and D. L. Williamson. A baroclinic instability test case for atmospheric model dynamical cores. *Quart. J. Roy. Meteor. Soc.*, 132:2943–2975, 2006.
[15] A. Kasahara. Numerical integration of the global barotropic primitive equations with hough harmonic expansions. *J. of the Atmos. Sci.*, 34(5):687–701, 1977.
[16] A. Kasahara. Further studies on a spectral model of the global barotropic primitive equations with hough harmonic expansions. *J. of the Atmos. Sci.*, 35(11):2043–2051, 1978.
[17] M.S. Longuet-Higgins. The eigenfunctions of Lalace's tidal equations over a sphere. *Phil. Trans. Roy. Soc. London*, 262(1132):511–607, 1968.
[18] T. Matsuno. Quasi-geostrophic motions in the equatorial area. *J. Meteorol Soc. Jpn*, 44:25–43, 1966.
[19] D. Müller and J.J. O'Brien. Shallow water waves on the rotating sphere. *Phys. Rev. E*, 51(2):4418–4431, 1995.
[20] N. Paldor. *Shallow Water Waves on the Rotating Earth*. Springer Brief in Earth System Sciences. Springer-Verlag, 2015.
[21] N. Paldor, Y. De-Leon, and O. Shamir. Planetary (Rossby) waves and inertia-gravity (poincaré) waves in a barotropic ocean over a sphere. *J. Fluid Mech.*, 726:123–136, 2013.
[22] B. Portelenelle and J.-P. Croisille. An efficient quadrature rule on the Cubed Sphere. *J. Comp. App. Math*, 328:59–74, 2018.
[23] R.J. Purser and M. Rancic. Smooth quasi-homogeneous gridding of the sphere. *J. Comput. Phys.*, 124:637–647, 1998.
[24] C. Jablonowski R. D. Nair. Moving vortices on the sphere: a test-case for horizontal advection problems. *Mon. Wea. Rev.*, 136:689–711, 2008.
[25] C. Ronchi, R. Iacono, and P. S. Paolucci. The Cubed Sphere: A new method for the solution of partial differential equations in spherical geometry. *J. Comput. Phys.*, 124:93–114, 1996.
[26] O. Shamir and N. Paldor. A Hermite-based shallow water solver for a thin ocean over a rotating sphere. *J. Comput. Phys.*, 269:80–97, 2014.
[27] O. Shamir and N. Paldor. A Gegenbauer-based shallow water solver for a thick ocean over a rotating sphere. *J. Comput. Phys.*, 304:487–505, 2016.
[28] O. Shamir and N. Paldor. A quantitative test case for global-scale dynamical cores based on analytic wave solutions of the shallow-water equations. *Quat. Jour. Roy. Met. Soc.*, 142:2705–2714, 2016.
[29] O. Shamir, I. Yacoby, S.Z. Ziv, and N. Paldor. The Matsuno baroclinic wave test case. *Geo. Scient. Dev.*, 12:2181–2193, 2019.
[30] J. Thuburn and Y. Li. Numerical simulation of Rossby-Haurwitz waves. *Tellus*, 52A:181–189, 2000.
[31] P. Ullrich, T. Melvin, C. Jablonowski, and A. Staniforth. A proposed baroclinic wave test case for deep- and shallow-atmosphere dynamical cores. *Quart. J. Roy. Meteor. Soc.*, 140:1590–1602, 2013.
[32] P. A. Ullrich, C. Jablonowski, and B. van Leer. High order finite-volume methods for the shallow-water equations on the sphere. *J. Comput. Phys.*, 229:6104–6134, 2010.
[33] P.A. Ullrich. *Atmospheric Modeling with High-Order finite volume methods*. PhD thesis, The Univ. of Michigan, 2011.
[34] D. L. Williamson. The evolution of dynamical cores for global atmospheric models. *J. Meteo. Soc. Japan*, 85B:241–269, 2007.
[35] D.L. Williamson, J.B. Drake, J.J. Hack, R. Jakob, and P. N. Swarztrauber. A standard test set for numerical approximations to the shallow water equations in spherical geometry. *J. Comput. Phys.*, 102:211–224, 1992.
[36] H.C. Yee and B. Sjögreen. Designing adaptive low-dissipative high-order schemes for long-time integrations. volume 66 of *Turbulent Flow Computation, Fluid Mechanics and its Applications*. Kluwer Acad. Pub., 2004.

†Univ. Grenoble Alpes, CNRS, Grenoble INP*, LJK, 38000 Grenoble, France, ‡Université de Lorraine, Département de Mathématiques, F-57045 Metz, France and C.N.R.S., Institut Elie Cartan de Lorraine, UMR 7502, F-57045 Metz, France

E-mail address: matthieu.brachet@inria.fr, jean-pierre.croisille@univ-lorraine.fr